Characteristic size effects on crystallographic structure and magnetic properties of $RMnO_3$ (R = Eu, Gd, Tb, Dy) nanoparticles

Takayuki Tajiri,*,† Hiroyuki Deguchi,‡ Masaki Mito,‡ and Atsushi Kohno†

†*Faculty of Science, Fukuoka University, Fukuoka 814-0180, Japan*

‡*Graduate School of Engineering, Kyushu Institute of Technology, Kitakyushu 804-8550, Japan*

E-mail: tajiri@fukuoka-u.ac.jp

Abstract

We synthesized lanthanoid manganese oxide $RMnO_3$ (R = Eu, Gd, Tb, and Dy) nanoparticles with particle sizes ranging from approximately 6.5 to 23 nm and investigated both their crystal structure and magnetic properties. The $RMnO_3$ nanoparticles showed a strong correlation between crystal structure and magnetic properties, and particle size effects on these properties vary owing to the different atomic radii of the lanthanoid ions. The magnetic properties of all the nanoparticles exhibited significant changes as the lattice constants changed at characteristic sizes that depend on the lanthanoid ionic radius; however, the characteristic size for magnetic properties corresponded to the magnitude of the orthorhombic distortion $b/a = 1.10$, regardless of the lanthanoid ionic radius. With decreasing particle size, $EuMnO_3$, $GdMnO_3$, and $TbMnO_3$ nanoparticles induced tensile strain of MnO_6 octahedra whereas compressive strain occurred in $DyMnO_3$ nanoparticles. The deformation of MnO_6 octahedra changed the magnetic interactions, resulting in changes in the magnetic properties. As

the particle size decreased, for R = Eu, Gd, and Tb, the magnetic properties, such as transition temperature, coercive field, and blocking temperature, decreased; conversely, these values increased in $DyMnO_3$. The distortion of the unit cell induced changes in the magnetic ordering state due to decreasing particle size.

Introduction

Orthorhombically distorted perovskite manganite $RMnO_3$ (R: lanthanoid) is well known as a strongly correlated electron material. $RMnO_3$ exhibits colossal magnetoresistance effect, multiferroic behavior, and distinctive magnetoelectric characteristics. The magnetic and electronic phases of $RMnO_3$ vary depending of the ionic radius of the lanthanoid. The magnitude of the Jahn–Teller distortion can be controlled by the substitution of the lanthanoid, while the orbital and magnetic structures of $RMnO_3$ depend strongly on the ionic radius of the lanthanoid.[1–11] As the ionic radius decreases, the magnetic ordering state at low temperatures changes from the A-type antiferromagnetic (A-AFM), to an incommensurate spin-cycloid, and then to the E-type antiferromagnetic (E-AFM) ordering state. In addition, the partial substitution of the lanthanoid induces changes in the magnetic state and transition temperature due to hole doping and the change in effective lanthanoid ion radius.[12–21] For R = La, Nd, and Sm, the lowest magnetic ordering state is A-AFM, and the Néel temperature T_N(Mn) ∼ 60–130 K decreases with decreasing ionic radius. $EuMnO_3$[8,13,14,17,22] and $GdMnO_3$[12,18,22,23] exhibit a phase transition from a paramagnetic to an A-AFM state below ∼ 45 and 25 K, respectively, via an incommensurate state with T_N(Mn) ∼ 50 and 43 K, respectively. The magnetic states of $TbMnO_3$[11,12,23,24] and $DyMnO_3$[19,20,23] change from paramagnetic to cycloidal spin order below ∼ 25 K via the incommensurate state below T_N(Mn) ∼ 40 K. For R = Ho, Er, Tm, Yb and Lu, the magnetic states change from paramagnetic to E-AFM via an incommensurate state below T_N(Mn) ∼ 40 K.[25,26] The magnetic phases and their transition temperatures depend on the Mn–O–Mn bond angles and Mn–O bond lengths in octahedral MnO_6, which vary according to the ionic radius of the lanthanoid. The decreas-

ing radius of the lanthanoid ion enhances the cooperative rotation of the MnO_6 octahedra ($GdFeO_3$-type distortion) causing a reduction in the Mn–O–Mn bond angles. In addition, the combination of orbital order and next-nearest-neighbor superexchange interactions has a nontrivial effect on the magnetic ground state in systems with orbital degeneracy and a large $GdFeO_3$-type distortion.[1,5,27–30] The distortion of the unit cell of $RMnO_3$ thin films due to epitaxial strain induces changes in the magnetic state and transition temperature.[31–37]

Because of the high proportion of surface atoms and finite size effects, nanoparticles possess unusual magnetic properties and crystal structures that differ from those of the bulk crystal. Nanoparticles of strongly correlated electron materials such as manganese oxide exhibit characteristic size effects on the crystal structure and magnetic properties owing to strong electron correlation and strong spin-orbit and spin-lattice coupling. Nanoparticles of strongly correlated materials, such as $LaMnO_3$,[38,39] $DyMnO_3$,[40] $GdMnO_3$,[41] $DyMn_2O_5$,[42] and NiO,[43] exhibit novel size effects on the magnetic properties and crystallographic structures, as already shown in our previous studies. These nanoparticles exhibit remarkable changes in crystal structure (i.e., on structural symmetry and lattice constants) and unique size effects on the magnetic properties. This study investigates on the size effects on the correlation between the magnetic properties and crystallographic structure of $RMnO_3$ (R = Eu, Gd, Tb, and Dy) nanoparticles, whose magnetic phase diagrams depend on the ionic radius of R. Emphasis was placed on the influence of atomic radius on the magnetic properties and crystal structures because of the variations in the magnetic state of the bulk crystals. The fact that $RMnO_3$ materials have the same crystal structure and their magnetic phase diagrams can be controlled by modulating the effective R ion radius by partial substitution of lanthanoids, $RMnO_3$ nanoparticles are an excellent testbed to study the effect of R ion size on magnetic properties. Previous studies have reported that nanoparticles of $DyMnO_3$ with particle size of 8.6–106 nm,[44,45] $GdMnO_3$ with particle size of 52–270 nm,[46–49] $TbMnO_3$ with particle size of 25 nm–3 μm[50–52] exhibited different behaviors from bulk crystals owing to changes in the particle size. In the case of $RMnO_3$ bulk crystals, the magnetic properties

and crystal structure have been investigated as a function of lanthanoid ionic radius, however, to the best of our knowledge, there have been no reports comparing size dependence of magnetic properties and crystal structure of $RMnO_3$ nanoparticles with similar particle size (approximately 10 nm) and different R ions. To clarify the size effects on the correlation between crystal structure and the magnetic properties of $RMnO_3$ (R = Eu, Gd, Tb, and Dy) nanoparticles, we conducted a systematic experimental study using the nanoparticle with same particle size region. We synthesized nanoparticles ranging in size from 6.5 to 23 nm. We herein report the size dependence of strong correlation between the crystal structure and the magnetic properties of $RMnO_3$ (R = Eu, Gd, Tb, and Dy) nanoparticles as well the effect of the magnetic ordering state of the bulk crystals on these size effects. In addition, these results provided a magnetic phase diagram of the nanoparticles as a function of lanthanoid ionic radius.

Experimental method

The $RMnO_3$ nanoparticles were synthesized in one-dimensional pores of mesoporous silica SBA-15 with a diameter of approximately 8 nm. SBA-15 has a well-ordered two-dimensional hexagonal mesoporous structure with one-dimensional pores separated by amorphous silica walls.[53] SBA-15 was used as a template to ensure equal particle size and prevent clumping of the synthesized nanoparticles. The $RMnO_3$ nanoparticles were synthesized by soaking SBA-15 in a stoichiometric aqueous solution of $R(CH_3COO)_3{\cdot}nH_2O$ and $Mn(CH_3COO)_2{\cdot}4H_2O$. The soaked SBA-15 samples were then dried and calcinated in an oxygen atmosphere.[40,41] The synthesis of $DyMnO_3$ nanoparticles in the pores of SBA-15 was confirmed via X-ray diffraction (XRD) and transmission electron microscopy (TEM). The mean particle size estimated from the TEM images was consistent with that obtained via XRD.[40] Previous studies have shown that the particle size of $LaMnO_3$,[38] $DyMn_2O_5$,[42] and NiO[43] nanoparticles synthesized in the pores of SBA-15 and obtained via XRD were consistent with the TEM

results. Therefore, it is reasonable to assume that, for the $TbMnO_3$, $GdMnO_3$, and $EuMnO_3$ nanoparticles also synthesized in the pores of SBA-15, the particle sizes estimated via XRD are valid. Therefore, XRD was used to estimate the particle sizes.

Powder XRD of the nanoparticles was conducted using a synchrotron radiation X-ray diffractometer with a Debye–Scherrer camera on the BL-8B beamline at the Photon Factory of the Institute of Materials Structure Science, High Energy Accelerator Research Organization (KEK). Incident X-rays with energy of 18 keV and a wavelength calibrated using the XRD pattern of CeO_2 powder were used. Figure1(a) shows the powder XRD patterns for each nanoparticle. The mean particle sizes of the $DyMnO_3$, $TbMnO_3$, $GdMnO_3$, and $EuMnO_3$ nanoparticles were estimated to be 14.8, 15.6, 16.0, and 16.8 nm, respectively. The diffraction patterns of all $RMnO_3$ nanoparticles exhibited broad Bragg peaks, which were attributed to an orthorhombic symmetry with space group *Pbnm*, identical to that of the $RMnO_3$ bulk crystals[7–9,54] shown in Fig. 1(b). The nanoparticles also contained the impurity R_2O_3 indicated by an asterisk in Fig. 1(a). The broad diffraction peaks were deconvoluted to those associated with $RMnO_3$ via multipeak fitting. The sizes of the $RMnO_3$ nanoparticles were estimated based on positions and full widths at half maximums of the Bragg peaks using the Scherrer equation. The XRD results confirmed the synthesis of $RMnO_3$ nanoparticles with sizes ranging from 6.5 to 23 nm. The lattice constants of the $RMnO_3$ nanoparticles were calculated from the relationship between the lattice constants and the plane indices determined from the Bragg peak angles of the deconvoluted peaks. The distortion of the MnO_6 octahedra was evaluated based on the assumption that the atomic positions of the nanoparticles were the same as in the bulk crystal. The Mn–O interatomic distances and the Mn–O–Mn bond angles were calculated using the lattice constants of the nanoparticles and the atomic position of the bulk crystal.[7,9]

The magnetic properties of the nanoparticles were investigated via a superconducting quantum interference device magnetometer (Quantum Design, Inc.). The DC magnetic susceptibilities were measured in an external magnetic field of 100 Oe under both field-

cooling (FC) and zero-field-cooling (ZFC) conditions. The AC susceptibility was measured in an AC magnetic field with frequencies ranging from 0.1 to 1000 Hz and an amplitude of 3.8 Oe. Magnetization curves up to 5 T were obtained at 15 K to avoid the effects of antiferromagnetic magnetic ordering of the lanthanoid in $RMnO_3$ at $T_N(R) \sim 7$ K.

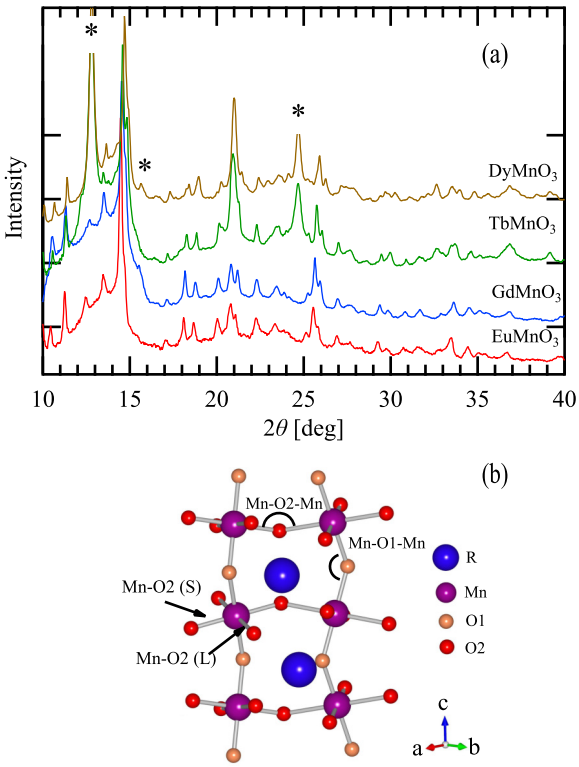

Figure 1: (a) Powder XRD patterns of $DyMnO_3$, $TbMnO_3$, $GdMnO_3$, and $EuMnO_3$ nanoparticles with particle sizes of 14.8, 15.6, 16.0, and 16.8 nm, respectively. The wavelength of the incident X-rays was 0.688 Å. The asterisks indicate the impurity phase R_2O_3. (b) Schematic of crystal structure with orthorhombic symmetry of $RMnO_3$.

Experimental results

$DyMnO_3$

Figure 2(a) shows the particle size dependence of the lattice constants a, b, and c, as well as the ratio of b to a for the $DyMnO_3$ nanoparticles. As the particle size decreased, the lattice constants a and c increased below the characteristic size of crystal structure $S_{c1}(\mathrm{Dy}) = 12.5$ nm and remained constant for particle size between 8 and 11.5 nm. Thereafter, the two lattice constants increased monotonically below $S_{c2}(\mathrm{Dy}) = 8.0$ nm. In contrast, the lattice constant b decreased with decreasing particle size, and showed two inflection points at $S_{c1}(\mathrm{Dy})$ and $S_{c2}(\mathrm{Dy})$ with decreasing particle size; however, the unit cell volume did not vary with particle size. The $DyMnO_3$ nanoparticles had a Jahn–Teller distorted orthorhombic structure (O'-type structure: $b > a > c\ /\sqrt{2}$). The orthorhombic distortion b/a of the nanoparticles with particle size less than 13 nm was smaller than that of the bulk crystal, $b/a = 1.105$.[7] The modulation of the orthorhombic distortion suggested changes in the symmetry of the MnO_6 octahedra with decreasing particle size and a Jahn–Teller distortion from those of the bulk crystal. The orthorhombic distortion of the $DyMnO_3$ nanoparticles exhibited a pronounced reduction below $S_{c2}(\mathrm{Dy})$. Above $S_{c2}(\mathrm{Dy})$, b/a remained essentially constant, but increased slowly with increasing particle size above $S_{c1}(\mathrm{Dy})$. These results suggest that the relaxation of orthorhombic distortion occurred once the particle size decreased below approximately $S_{c1}(\mathrm{Dy})$ and was significant below $S_{c2}(\mathrm{Dy})$. Figure 2(b) shows the size dependence of the Mn–O bond lengths of the MnO_6 octahedra in the $DyMnO_3$ nanoparticles. The MnO_6 octahedra have three distinct M–O bond lengths, Mn–O1, Mn–O2(S), and Mn–O2(L) (Fig. 1(b)). The size dependences of all Mn–O bond lengths exhibited pronounced changes at $S_{c1}(\mathrm{Dy})$ and $S_{c2}(\mathrm{Dy})$. As particle size decreased, the Mn–O1 bond length increased for particle sizes below approximately 11 nm, remained constant for sizes between 8 and 11 nm, and then increased for sizes below $S_{c2}(\mathrm{Dy})$. In contrast, the Mn–O2(L) bond length decreased with decreasing particle size and exhibited two inflection points at approximately

8 and 11 nm. The Mn–O2(L) bond length remained essentially constant at particle sizes ranging from 8 to 10 nm and above 12 nm. Mn–O2(S) exhibited a similar behavior to that of Mn–O2(L), however, the bond length of Mn–O2(S) increased with decreasing particle size for particle sizes above S_{c1}(Dy). These results indicate that, as particle size decreased, the MnO_6 octahedra compressed along the *ab*-plane and expanded along the *c*-axis, that is, the $DyMnO_3$ nanoparticles displayed compressive strain, particularly in particle sizes below S_{c2}(Dy). Figure 2(c) shows the relationship between the Mn–O–Mn bond angles and particle size for $DyMnO_3$ nanoparticles. The two bond angles exhibited pronounced changes at approximately S_{c1}(Dy) and S_{c2}(Dy). As particle size decreased, the Mn–O1–Mn and Mn–O2–Mn bond angles increased and decreased, respectively.

Figure 2(d) shows the temperature dependence of the DC susceptibility of $DyMnO_3$ nanoparticles with a particle size of 11.3 nm. Both the FC and ZFC susceptibilities of the nanoparticles increased below approximately 45 K because of the antiferromagnetic ordering of Mn magnetic moments, which corresponds to T_N(Mn) $\sim$ 39 K for $DyMnO_3$ bulk crystal.[19,20,23] In this bulk crystal, Dy spins order antiferromagnetically below a T_N(Dy) $\sim$ 6 K[2,19,20,23] and the paramagnetic susceptibility of the Dy spins mask the antiferromagnetic transition of the Mn sublattice.[20] The rapid increase in both FC and ZFC susceptibilities below 10 K is attributed to the antiferromagnetic ordering of the Dy spins in the $DyMnO_3$ nanoparticles. In addition, the existence of paramagnet Dy_2O_3 may affect the increase in both FC and ZFC susceptibilities below 10 K. A pronounced magnetic irreversibility between the FC and ZFC susceptibilities was observed below $T_{irr} = 36$ K as indicated by the lower arrow in Fig. 2(d). The ZFC susceptibility exhibited a hump at approximately 20 K. The appearances of irreversibility and a peak of ZFC susceptibility are the characteristic behaviors of superparamagnetics. For superparamagnetic nanoparticles, typically, the FC susceptibility is constantly increasing like in paramagnetism, whereas the ZFC susceptibility exhibits a peak at the blocking temperature because of the existence of activation energy for the reversal of the magnetic moments. It then decreases toward zero with decreasing

temperature. AC susceptibility exhibits a peak at the blocking temperature.[55] The ZFC susceptibility of $DyMnO_3$ nanoparticles exhibited a hump owing to the blocking phenomena and increased due to the paramagnetic susceptibility of Dy spins in $DyMnO_3$ nanoparticles and Dy_2O_3 with decreasing temperature. The temperature at the appearance of the hump in ZFC susceptibility corresponded to the blocking temperature obtained by AC susceptibility as shown in Fig. 2(f). These behaviors are consistent with the blocking phenomena of superparamagnetism. The upper panel of Fig. 2(e) shows the size dependence of $T_{\rm irr}$, which displayed a constant value above characteristic size of magnetic property $S_{\rm m1}({\rm Dy}) =$ 11.4 nm, rapidly decreased at $S_{\rm m1}({\rm Dy})$, and increased linearly with decreasing particle size below $S_{\rm m2}({\rm Dy}) = 8.2$ nm. The AC susceptibility of the $DyMnO_3$ nanoparticles was measured in the frequency range of 0.1–1000 Hz. Figure 2(f) shows the temperature dependence of the AC susceptibility of the $DyMnO_3$ nanoparticles with a particle size of 11.3 nm at 100 Hz. Both the in-phase (χ') and the out-of-phase susceptibilities (χ'') of the nanoparticles increased below approximately 40 K and peaked at the blocking temperature ($T_{\rm B}$). The peaks of both $\chi'(T)$ and $\chi''(T)$ shifted toward higher temperatures with increasing frequency. This relaxation behavior is indicative of superparamagnetic behavior. $T_{\rm B}$ at 100 Hz remained nearly constant above $S_{\rm m1}({\rm Dy})$. Below $S_{\rm m1}({\rm Dy})$, $T_{\rm B}$ increased with decreasing particle size and remained almost constant between $S_{\rm m1}({\rm Dy})$ and $S_{\rm m2}({\rm Dy})$. $T_{\rm B}$ increased below $S_{\rm m2}({\rm Dy})$ (middle panel, Fig. 2(e)). Figure 2(g) shows the magnetization curve of $DyMnO_3$ nanoparticles with a particle size of 11.3 nm at 15 K which was lower than the $T_{\rm B}$. The superparamagnetic behaviors show a hysteresis loop in the magnetization curve below blocking temperature, whereas they show a paramagnetic-like behavior without a hysteresis loop above $T_{\rm B}$. In addition, the magnetization is described by a Langevin function. In fact, the $DyMnO_3$ nanoparticles exhibited a hysteresis loop in the magnetization curves below the blocking temperature and their magnetization curves were reproduced by a Langevin function for isolated spin assembly.[40] $H_{\rm c}$ at 15 K was essentially constant above $S_{\rm m1}({\rm Dy})$ and increased rapidly with decreasing particle size below $S_{\rm m1}({\rm Dy})$ (bottom panel, Fig. 2(e)). The

magnetic measurements indicate that the magnetic properties of the $DyMnO_3$ nanoparticles changed significantly at S_{m1}(Dy) and their magnetic parameters increased with decreasing particle size below S_{m1}(Dy).

$TbMnO_3$

Figure 3(a) shows the particle size dependence of the lattice constants a, b, and c, as well as b/a of the $TbMnO_3$ nanoparticles. Above S_c(Tb) = 15.8 nm, these values were essentially constant. As the particle size decreased, a and b increased, while the c decreased. The size dependences of the lattice constants of the $TbMnO_3$ nanoparticles differed from those of the $DyMnO_3$ nanoparticles shown in Fig. 2(a). Similar to the $DyMnO_3$ nanoparticles, the unit cell volume of the $TbMnO_3$ nanoparticles did not change with particle size. The $TbMnO_3$ nanoparticles had a Jahn–Teller distorted orthorhombic structure, similar to the $DyMnO_3$ nanoparticles. The orthorhombic distortion b/a remained essentially constant above S_c(Tb) and increased monotonically with decreasing particle size below S_c(Tb). These results indicate that the size dependence of the orthorhombic distortion of the $TbMnO_3$ nanoparticles was the opposite of that of the $DyMnO_3$ nanoparticles. Figure 3(b) shows the size dependence of the bond lengths of the MnO_6 octahedra in the $TbMnO_3$ nanoparticles. The size dependence of the Mn–O bond lengths exhibited a pronounced change at S_c(Tb) and remained constant above S_c(Tb). As particle size decreased, the Mn–O1 bond length decreased, while the Mn–O2(L) and Mn–O2(S) bond lengths increased. These results indicate that the MnO_6 octahedra expanded along the ab-plane and contracted along the c-axis, that is, tensile strain occurred as particle size decreased below S_c(Tb), which is the opposite behavior to that of $DyMnO_3$ nanoparticles that display compressive strain. Figure 3(c) shows the size dependences of the Mn–O–Mn bond angles of the $TbMnO_3$ nanoparticles. The two bond angles, Mn–O1–Mn and Mn–O2–Mn, were identical at 145.2°, and displayed constant values above approximately S_c(Tb). The two values diverged with decreasing particle size below S_c(Tb). Below S_c(Tb), the Mn–O1–Mn and Mn–O2–Mn bond angles decreased and

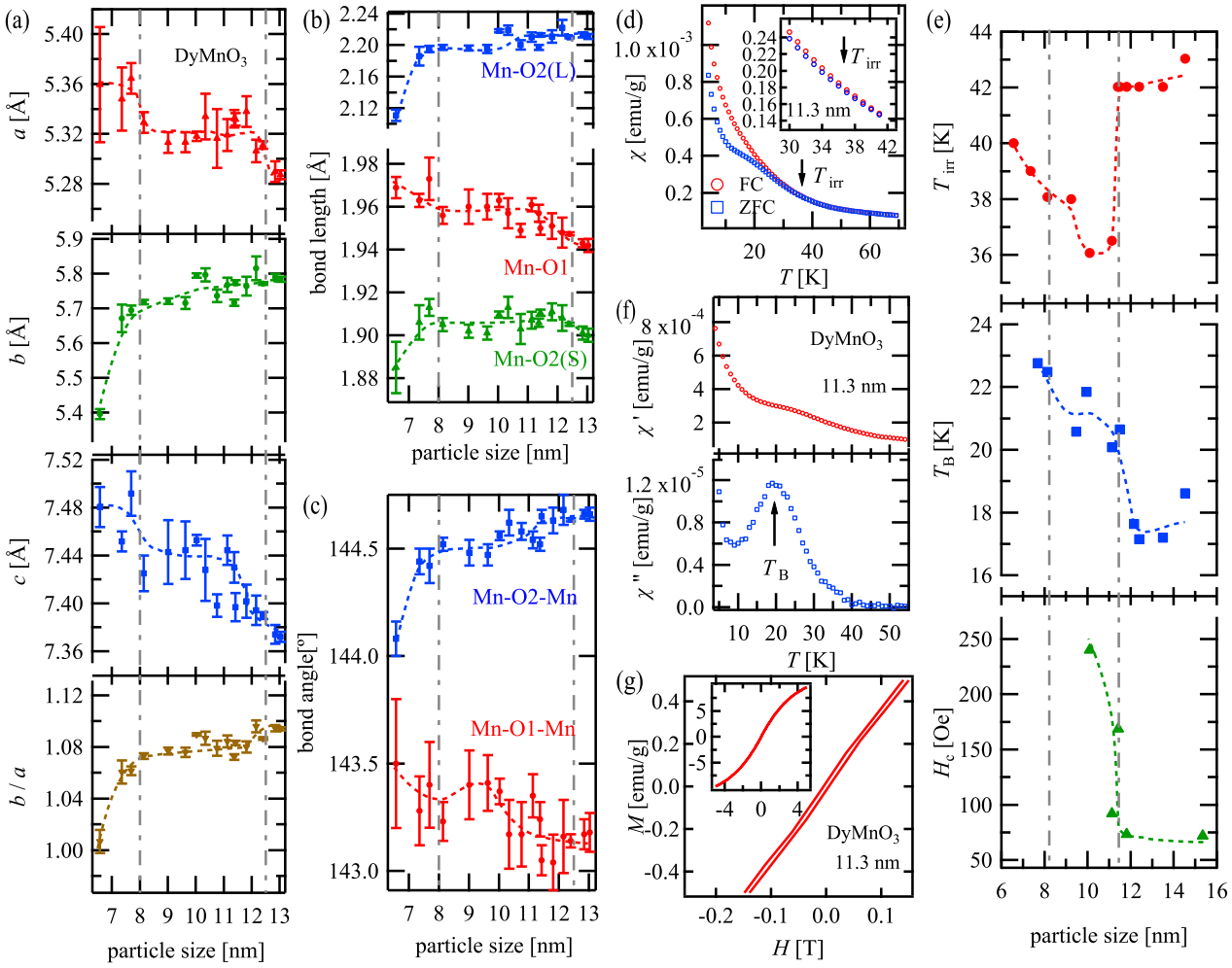

Figure 2: Particle size dependence of (a) lattice constants a, b, c, and b/a, (b) the Mn–O bond lengths, and (c) Mn–O–Mn bond angles of the $DyMnO_3$ nanoparticles. Vertical dashed lines indicate the characteristic size, $S_{c1}(\mathrm{Dy}) = 12.5$ nm and $S_{c2}(\mathrm{Dy}) = 8.0$ nm. The bond lengths and bond angles were calculated using the lattice constants of the nanoparticles and the atomic position of the bulk crystal. Positional relationship of the three bond lengths and two bond angles are shown in Fig. 1(b). (d) Temperature dependence of DC magnetic susceptibilities of $DyMnO_3$ nanoparticles with a particle size of 11.3 nm in an external magnetic field of 100 Oe under FC (red circular symbols) and ZFC (blue square symbols) conditions. Inset shows magnified view around the T_{irr} as indicated by allow. (e) Particle size dependences of T_{irr}, T_{B}, and H_{c} of the $DyMnO_3$ nanoparticles. Vertical dashed lines indicate the characteristic size, $S_{m1}(\mathrm{Dy}) = 11.4$ nm and $S_{m2}(\mathrm{Dy}) = 8.2$ nm. (f) Temperature dependence of in-phase (upper panel) and out-of-phase (lower panel) susceptibilities of $DyMnO_3$ nanoparticles with a particle size of 11.3 nm at a frequency of 100 Hz in a zero DC field. Arrow indicates the T_{B} (g) Magnified low field region of the magnetization curve of $DyMnO_3$ nanoparticles with a particle size of 11.3 nm at 15 K. Inset shows overview of this magnetization curve ranging from -5 to 5 T.

increased monotonically, respectively, with decreasing particle size. The size dependences of the Mn–O–Mn bond angles of the $TbMnO_3$ nanoparticles differed from those of the $DyMnO_3$ nanoparticles shown in Fig. 2(c).

Figure 3(d) shows the temperature dependence of the DC susceptibility of $TbMnO_3$ nanoparticles with a particle size of 14.7 nm. Both the FC and ZFC susceptibilities of the nanoparticles increased below approximately 40 K, which was attributed to the antiferromagnetic ordering of Mn magnetic moments in the nanoparticles. The temperature corresponded to a $T_N(\mathrm{Mn}) \sim 42$ K in $TbMnO_3$ bulk crystal.[11,12,23,24] The rapid increase in both FC and ZFC susceptibilities below 10 K was attributed to the antiferromagnetic ordering of the Tb spins in $TbMnO_3$, which orders at $T_N(\mathrm{Tb}) \sim 7$ K.[2,23,24] The existence of paramagnet Tb_2O_3 affected the increase in both FC and ZFC susceptibilities below 10 K. A pronounced magnetic irreversibility between FC and ZFC susceptibilities was observed below $T_{irr} = 45$ K as indicated by an arrow in Fig. 3(d). The ZFC susceptibility exhibited a hump at approximately 20 K which corresponded to the T_B obtained by AC susceptibility (Fig. 3(f)). The temperature dependence of DC susceptibilities of $TbMnO_3$ nanoparticles were similar to those of the $DyMnO_3$ nanoparticles. T_{irr} of the $TbMnO_3$ nanoparticles varied with particle size as shown in Fig. 3(e). Above $S_m(\mathrm{Tb}) = 15.6$ nm, T_{irr} was essentially constant at 64 K. Below $S_m(\mathrm{Tb})$, T_{irr} decreased significantly and then remained at a constant value of 41 K below approximately 14 nm. The significant decrease in T_{irr} at around $S_c(\mathrm{Tb})$ corresponded to that of the $DyMnO_3$ nanoparticles; however, the $TbMnO_3$ nanoparticles did not exhibit an increase in T_{irr} below $S_m(\mathrm{Tb})$. The abrupt change in T_{irr} at $S_m(\mathrm{Tb})$ is consistent with the change the $TbMnO_3$ nanoparticles at $S_c(\mathrm{Tb})$. The AC susceptibility of the $TbMnO_3$ nanoparticles was measured in the frequency range of 1–1000 Hz. Both χ' and $\chi''$of the $TbMnO_3$ nanoparticles increased below approximately 40 K and peaked at T_B. The peaks of both $\chi'(T)$ and $\chi''(T)$ shifted toward higher temperatures with increasing frequency. The observed relaxation was attributed to superparamagnetic behavior. Figures 3(f) and (e) show the temperature dependence of the AC susceptibility and the size depen-

dence of T_{B}, respectively, at 100 Hz. T_{B} maintained nearly constant above approximately S_{m}(Tb). Below S_{m}(Tb), T_{B} decreased with decreasing particle size. Figure 3(g) shows the magnetization curve of $TbMnO_3$ nanoparticles with a particle size of 13.6 nm at 15 K. The magnetization exhibited a hysteresis loop owing to superparamagnetism, which was similar to that of the $DyMnO_3$ nanoparticles. H_{c} was essentially constant above S_{m}(Tb) and then decreased rapidly at S_{m}(Tb) as shown in Fig. 3(e). As particle size decreased, H_{c} decreased monotonically below S_{m}(Tb). The size dependence of H_{c} corresponded to that of T_{irr} and T_{B}. T_{B} and H_{c} of the $TbMnO_3$ nanoparticles exhibited opposite tendencies to those of the $DyMnO_3$ nanoparticles. The differences in size dependence of magnetic properties were attributed to the changes in crystal structure. The details of those behaviors are described later in the Discussion section.

$GdMnO_3$

The size dependence of the lattice constants and orthorhombic distortion of the $GdMnO_3$ nanoparticles are shown in Fig. 4(a). With decreasing particle size, the estimated lattice constants a and b increased whereas c decreased. The size dependence of the lattice constants of the $GdMnO_3$ nanoparticles were similar to those of $TbMnO_3$, but differed from those of $DyMnO_3$. The lattice constant a was almost constant above S_{c1}(Gd) = 19.5 nm and increased slightly with decreasing particle size below S_{c1}(Gd). The maximum value of b was observed at S_{c1}(Gd) and remained constant between 14 and 18 nm. Below S_{c2}(Gd) = 13.9 nm, b increased monotonically with decreasing particle size, while c decreased with particle size below S_{c2}(Gd). Similar to the $DyMnO_3$ and $TbMnO_3$ nanoparticles, the unit cell volume did not depend on the particle size. The relationship between the magnitudes of the lattice constants indicated that the $GdMnO_3$ nanoparticles had a Jahn–Teller distorted orthorhombic structure. The orthorhombic distortion b/a increased with decreasing particle size below S_{c2}(Gd) and exhibited a maximum value at S_{c1}(Gd). The size dependence of b/a of the $GdMnO_3$ nanoparticles was similar to that of the $TbMnO_3$ nanoparticles, except for

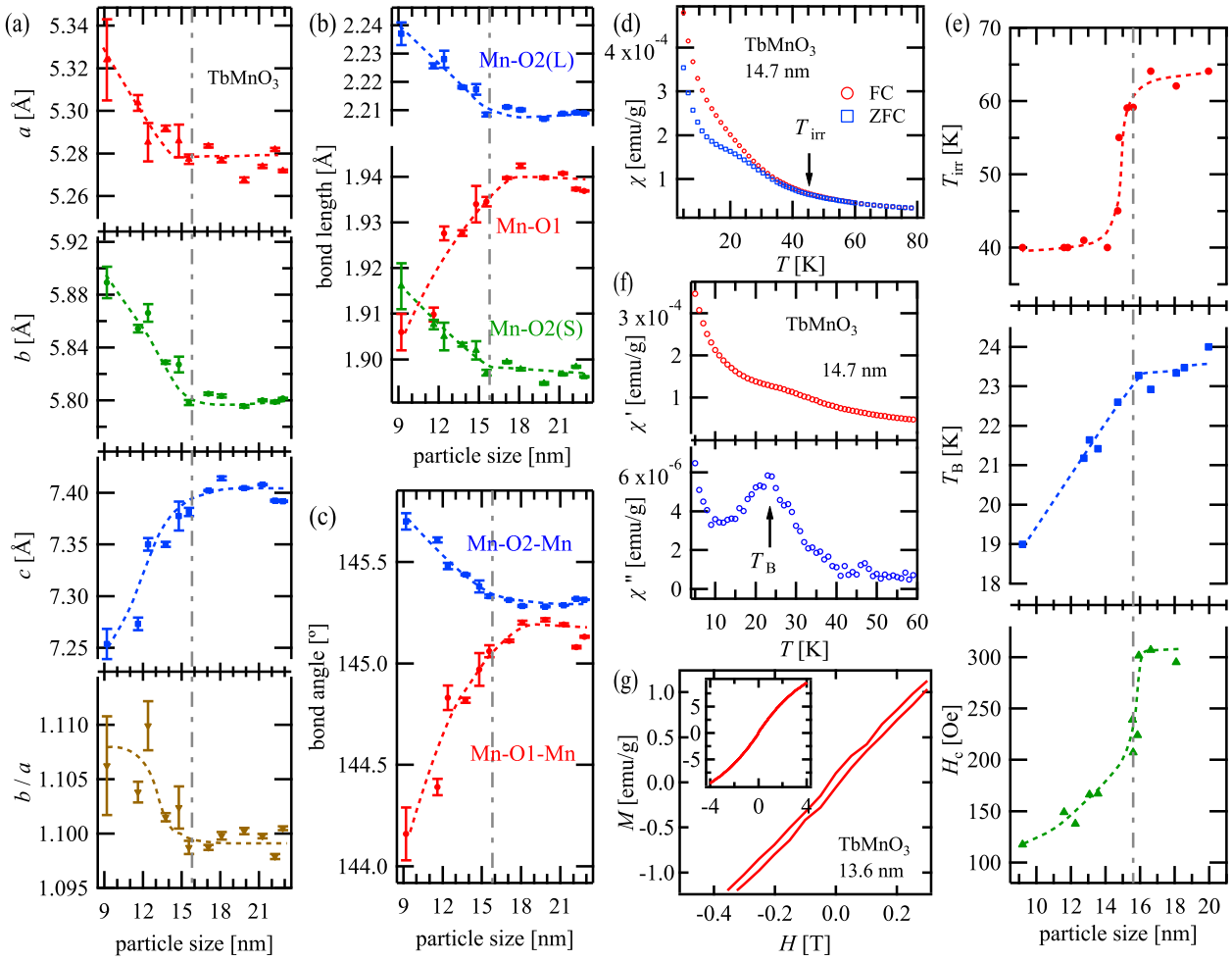

Figure 3: Particle size dependence of (a) lattice constants a, b, c, and b/a, (b) the Mn–O bond lengths, and (c) Mn–O–Mn bond angles of the $TbMnO_3$ nanoparticles. Vertical dashed lines indicate the characteristic size, $S_c(\mathrm{Tb}) = 15.8$ nm. The bond lengths and bond angles were calculated using the lattice constants of the nanoparticles and the atomic position of the bulk crystal. (d) Temperature dependence of DC magnetic susceptibilities of $TbMnO_3$ nanoparticles with a particle size of 14.7 nm in an external magnetic field of 100 Oe under FC and ZFC conditions. Arrow indicates the T_{irr}. (e) Particle size dependences of T_{irr}, T_{B}, and H_c of the $TbMnO_3$ nanoparticles. Vertical dashed lines indicate the characteristic size, $S_m(\mathrm{Tb}) = 15.6$ nm. (f) Temperature dependence of χ' and $\chi''$of $TbMnO_3$ nanoparticles with a particle size of 14.7 nm at a frequency of 100 Hz in a zero DC field. Arrow indicates the T_{B}. (g) Magnified low field region of the magnetization curve of $TbMnO_3$ nanoparticles with a particle size of 13.6 nm at 15 K. Inset shows overview of this magnetization curve ranging from -4 to 4 T.

existence of a hump at S_{c1}(Gd). Figure 4(b) shows the size dependence of the bond lengths of the MnO_6 octahedra of the $GdMnO_3$ nanoparticles. The size dependences of the Mn–O1 and Mn–O2(L) bond lengths exhibited pronounced changes at S_{c2}(Gd) and remained constant above S_{c2}(Gd). As particle size decreased, the Mn–O1 bond length decreased, while the Mn–O2(L) bond length increased below S_{c2}(Gd). The Mn–O2(S) bond length exhibited a gradual increase with decreasing particle size with two inflection points at S_{c1}(Gd) and S_{c2}(Gd). The MnO_6 octahedra expanded along the *ab*-plane and contracted along the *c*-axis with decreasing particle size, which indicated the presence of tensile strain, similar to the $TbMnO_3$ nanoparticles. The size dependence of the Mn–O–Mn bond angles of the $GdMnO_3$ nanoparticles is shown in Fig. 4(c). The two bond angles had identical values of 145.8° above approximately S_{c1}(Gd); however, the two bond angles diverged with decreasing particle size below S_{c1}(Gd). The Mn–O2–Mn bond angles remained constant above S_{c1}(Gd) and the Mn–O2–Mn bond angle increased monotonically with decreasing particle size below S_{c1}(Gd). In contrast, the Mn–O1–Mn bond angle remained constant above approximately S_{c1}(Gd) and began to decrease below approximately S_{c1}(Gd). Thereafter, the Mn–O1–Mn bond angle exhibited a significant decrease below 11 nm. The size dependence of the Mn–O–Mn bond angles of the $GdMnO_3$ nanoparticles were similar to those of the $TbMnO_3$ and differed from those of $DyMnO_3$.

Figure 4(d) shows the temperature dependence of the DC susceptibility of $GdMnO_3$ nanoparticles with a size of 19.7 nm. Both the FC and ZFC susceptibilities of the $GdMnO_3$ nanoparticles increased below approximately 40 K, which was attributed to the antiferromagnetic ordering of Mn magnetic moments in the nanoparticles. The temperature corresponded to the T_N(Mn) $\sim$ 43 K for $GdMnO_3$ bulk crystal.[12,18,22,23] The rapid increase in both FC and ZFC susceptibilities below 10 K was attributed to the antiferromagnetic ordering of the Gd spins at T_N(Gd) $\sim$ 8 K[2,18,22,23] in the $GdMnO_3$ nanoparticles and was affected by the presence of the paramagnet Gd_2O_3 phase. The ZFC susceptibility exhibited a maximum at approximately 39 K which corresponded to the T_B obtained by AC susceptibility (Fig. 4(f)).

In contrast to the susceptibilities of the $DyMnO_3$ and $TbMnO_3$ nanoparticles, both the FC and ZFC susceptibilities increased rapidly at approximately 40 K. The rapid increase in the susceptibilities of the $GdMnO_3$ nanoparticles corresponded to ferromagnetic ordering similar to that displayed by $LaMnO_3$ nanoparticles,[38] where the $LaMnO_3$ bulk crystal exhibits an A-type antiferromagnetic ordering below T_N, similar to the $GdMnO_3$ bulk crystal. The pronounced increase in both the FC and ZFC susceptibilities at approximately 40 K because of the ferromagnetic-like behavior did not occur in particle with sizes below 14 nm. $GdMnO_3$ nanoparticles with a particle size less than $S_{m2}(Gd) = 14.0$ nm exhibited pronounced changes in their crystal lattice parameters. A pronounced magnetic irreversibility between FC and ZFC susceptibilities was observed below $T_{irr} = 61$ K. T_{irr} varied with particle size (upper panel, Fig. 4(e)). T_{irr} decreased rapidly at $S_{m1}(Gd) = 20.1$ nm and remained constant at $T_{irr} = 55$ K in the 14–18 nm range. Thereafter, T_{irr} decreased monotonically below $S_{m2}(Gd)$. The abrupt changes in T_{irr} at $S_{m1}(Gd)$ and $S_{m2}(Gd)$ were consistent with the crystal lattice parameters of the $GdMnO_3$ nanoparticles at both $S_{c1}(Gd) = 19.5$ nm and $S_{c2}(Gd) = 13.9$ nm.

The AC susceptibility of the $GdMnO_3$ nanoparticles was measured in the frequency range of 1–1000 Hz. Both χ' and χ''increased below approximately 40 K and peaked at the blocking temperature T_B. The $GdMnO_3$ nanoparticles exhibited relaxation phenomena owing to superparamagnetic behavior, similar to the $DyMnO_3$ and $TbMnO_3$ nanoparticles. Figure 4(f) shows the temperature dependence of the AC susceptibility at 100 Hz for a particle size of 19.7 nm. T_B at 100 Hz exhibited a size dependence similar to that of T_{irr} as shown in middle panel of Fig. 4(e). T_B was essentially constant above $S_{m1}(Gd)$, decreased rapidly at $S_{m1}(Gd)$, remained constant between 14 and 18 nm, and then decreased monotonically below $S_{m2}(Gd)$. Figure 4(g) shows the magnetization curve of $GdMnO_3$ nanoparticles with a particle size of 17.3 nm at 15 K. A hysteresis loop owing to superparamagnetic behavior was observed. H_c at 15 K decreased rapidly at a particle size of approximately $S_{m1}(Gd)$. As particle size decreased further, H_c remained constant between 14 and 18 nm, then decreased

below S_{m2}(Gd). As shown in bottom panel of Fig. 4(e), the size dependence of H_c was similar to that of T_{irr} and T_B. The size dependence of the magnetic properties of the $GdMnO_3$ nanoparticles exhibited a similar tendency to those of the $TbMnO_3$ nanoparticles.

$EuMnO_3$

The lattice constants and orthorhombic distortion of the $EuMnO_3$ nanoparticles depended on the particle size, as shown in Fig. 5(a). The lattice constant a did not exhibit a significant change below 21 nm. As the particle size decreased, the lattice constant b increased significantly above S_{c1}(Eu) = 19.7 nm, then exhibited a moderate increase between approximately 14 and 20 nm. Below S_{c2}(Eu) = 14.8 nm, b increased rapidly at S_{c2}(Eu) and exhibited a monotonical increase with decreasing particle size. In contrast, the lattice constant c remained constant above S_{c2}(Eu), decreased rapidly at S_{c2}(Eu), then decreased slightly with a further decrease in particle size. The unit cell volume did not vary with the particle size similar to other three nanoparticles, which suggests that the distortion of unit cell of all the nanoparticles was enhanced with decreasing particle size. The $EuMnO_3$ nanoparticles had a Jahn–Teller distorted orthorhombic structure. The orthorhombic distortion b/a increased with decreasing particle size below approximately S_{c2}(Eu); however, b/a remained constant above approximately S_{c2}(Eu). Figure 5(b) shows the size dependence of the bond lengths of the MnO_6 octahedra of the $EuMnO_3$ nanoparticles. The bond lengths Mn–O1, M–O2(S), and Mn–O2(L) exhibited pronounced changes at both S_{c1}(Eu) and S_{c2}(Eu). As the particle size decreased, the Mn–O1 bond length decreased, while the Mn–O2(S) and Mn–O(L) bond lengths increased. These results indicate that the MnO_6 octahedra expanded along the ab-plane and contracted along the c-axis with decreasing particle size, that is, tensile strain occurred, similar to the $TbMnO_3$ nanoparticles. Figure 5(c) shows the size dependence of the Mn–O–Mn bond angles for the $EuMnO_3$ nanoparticles. The two bond angles, Mn–O1–Mn and Mn–O2–Mn, were both 146.45° above S_{c2}(Eu), but exhibited a pronounced change at approximately S_{c2}(Eu). The Mn–O1 –Mn bond angle began to decrease at S_{c2}(Eu) and

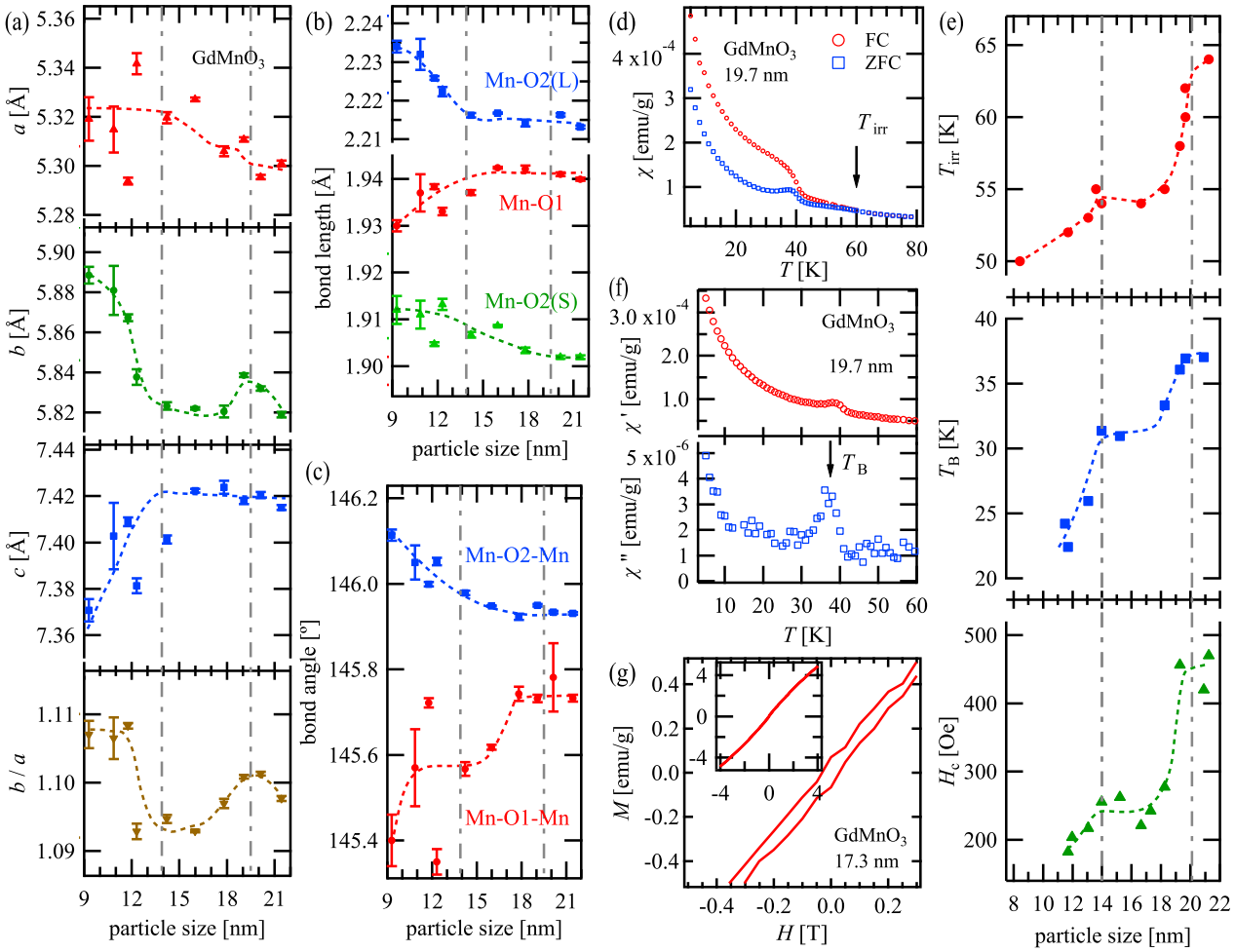

Figure 4: Particle size dependence of (a) lattice constants a, b, c, and b/a, (b) calculated Mn–O bond lengths, and (c) Mn–O–Mn bond angles of the $GdMnO_3$ nanoparticles. Vertical dashed lines indicate the characteristic size, $S_{c1}(\mathrm{Gd}) = 19.5$ nm and $S_{c2}(\mathrm{Gd}) = 13.9$ nm. (d) Temperature dependence of DC magnetic susceptibilities of $GdMnO_3$ nanoparticles with a particle size of 19.7 nm in an external magnetic field of 100 Oe under FC and ZFC conditions. Arrow indicates the T_{irr}. (e) Particle size dependences of T_{irr}, T_{B}, and H_{c} of the $GdMnO_3$ nanoparticles. Vertical dashed lines indicate the characteristic size, $S_{m1}(\mathrm{Gd}) = 20.1$ nm and $S_{m2}(\mathrm{Gd}) = 14.0$ nm. (f) Temperature dependence of χ' and $\chi''$of $GdMnO_3$ nanoparticles with a particle size of 19.7 nm at a frequency of 100 Hz in a zero DC field. Arrow indicates the T_{B}. (g) Magnetization curve up to 4 T of $GdMnO_3$ nanoparticles with a particle size of 17.3 nm at 15 K.

asymptotically approached 146.15°, while the Mn–O2–Mn bond angle increased rapidly at S_{c2}(Eu) and was essentially constant at 146.6° below 13 nm. The values of the two bond angles intersected at approximately 14 nm.

Figure 5(d) shows temperature dependence of the DC susceptibility of $EuMnO_3$ nanoparticles with a particle size of 15.4 nm. Both the FC and ZFC susceptibilities increased below approximately 40 K, which was attributed to the antiferromagnetic ordering of Mn magnetic moments in the nanoparticles. The temperature corresponded to T_N(Mn) $\sim$ 50 K for $EuMnO_3$ bulk crystal.[8,13,14,17,22] Both FC and ZFC susceptibilities increased monotonically owing to the paramagnetic susceptibility of Eu_2O_3. A pronounced magnetic irreversibility between FC and ZFC susceptibilities was observed below T_{irr} = 54 K. The ZFC susceptibility exhibited a hump at approximately 30 K, which corresponded to the T_B obtained by AC susceptibility (Fig. 5(f)). For particle sizes larger than 15 nm, the $EuMnO_3$ nanoparticles exhibited ferromagnetic ordering behavior at approximately 40 K, similar to the $GdMnO_3$ nanoparticles. At particle size less than S_m(Eu) = 15.3 nm, the crystal lattice parameters of the $EuMnO_3$ nanoparticles exhibited pronounced changes and differed significantly from those above S_{c2}(Eu) = 14.8 nm. T_{irr} decrease rapidly below S_m(Eu), but remained almost constant above S_m(Eu) (upper panel, Fig. 5(e)). The size dependence of T_{irr} was similar to that of b/a. The AC susceptibility of the $EuMnO_3$ nanoparticles was determined in the frequency range of 1–1000 Hz. Both χ' and χ''increased below approximately 40 K and peaked at the blocking temperature T_B. The $EuMnO_3$ nanoparticles exhibited relaxation phenomena consistent with superparamagnetic behavior. Figure 5(f) shows the temperature dependence of the AC susceptibility at 100 Hz for $EuMnO_3$ nanoparticles with a size of 15.4 nm. T_B decreased rapidly at approximately S_m(Eu) and remained essentially constant below approximately 14 nm (middle panel, Fig. 5(e)). This size dependence was similar to that of the T_{irr} of the $EuMnO_3$ nanoparticles. The magnetization curve of $EuMnO_3$ nanoparticles with a particle size of 15.5 nm exhibited a hysteresis loop owing to superparamagnetism at 15 K (Fig. 5(g)). The magnetization increased rapidly at around H_c, which is different

from the behavior of the $DyMnO_3$, $TbMnO_3$, and $GdMnO_3$ nanoparticles. In addition, the H_c of $EuMnO_3$ nanoparticles was more than double that of the other three nanoparticles. These results suggest that the difference in the magnetization curves is attributable to the magnetic phase of the bulk crystal at low temperatures, where the lowest magnetic ordering state of $EuMnO_3$ and $GdMnO_3$ bulk crystals is the A-type antiferromagnetic state. H_c at 15 K varied with particle size as shown in the bottom panel of Fig. 5(e). As the particle size decreased, H_c remained essentially constant above S_m(Eu), rapidly decreased at S_m(Eu), then remained constant below 14 nm. The size dependence of H_c was similar to that of T_{irr} and T_B. The size dependences of magnetic properties of $EuMnO_3$ nanoparticles displayed similar behavior to those of $TbMnO_3$ and $GdMnO_3$.

Discussion

The dependence of the lattice constants, bond angles, and bond lengths on the lanthanoid ionic radii for particles with a size of 10 nm was determined for each nanoparticle. Figure 6 shows the lattice constants, bond lengths, and bond angles as a function of ionic radius. The lattice constants a and b, and the ratio of b/a, decreased with decreasing ionic radius, while the lattice constant c exhibited a minimum at 1.10 Åfor Tb. The trends in the lattice constants and the deformation of MnO_6 octahedra of the $EuMnO_3$ and $TbMnO_3$ nanoparticles were qualitatively the same as those of the bulk crystals. The lattice constants b, c, b/a, and bond lengths of the $DyMnO_3$ nanoparticles were significantly different from those of the other three compounds. The reduction in orthorhombic distortion with deceasing ionic radius was the opposite behavior to that of the bulk crystals. The difference in orthorhombic distortion between the nanoparticles and bulk crystals is significant. The changes in the crystal lattice parameters of nanoparticles with changing ionic radius were larger than those of the bulk crystals, indicating that the nanoparticles were more sensitive to changes in ionic radius than bulk crystals.

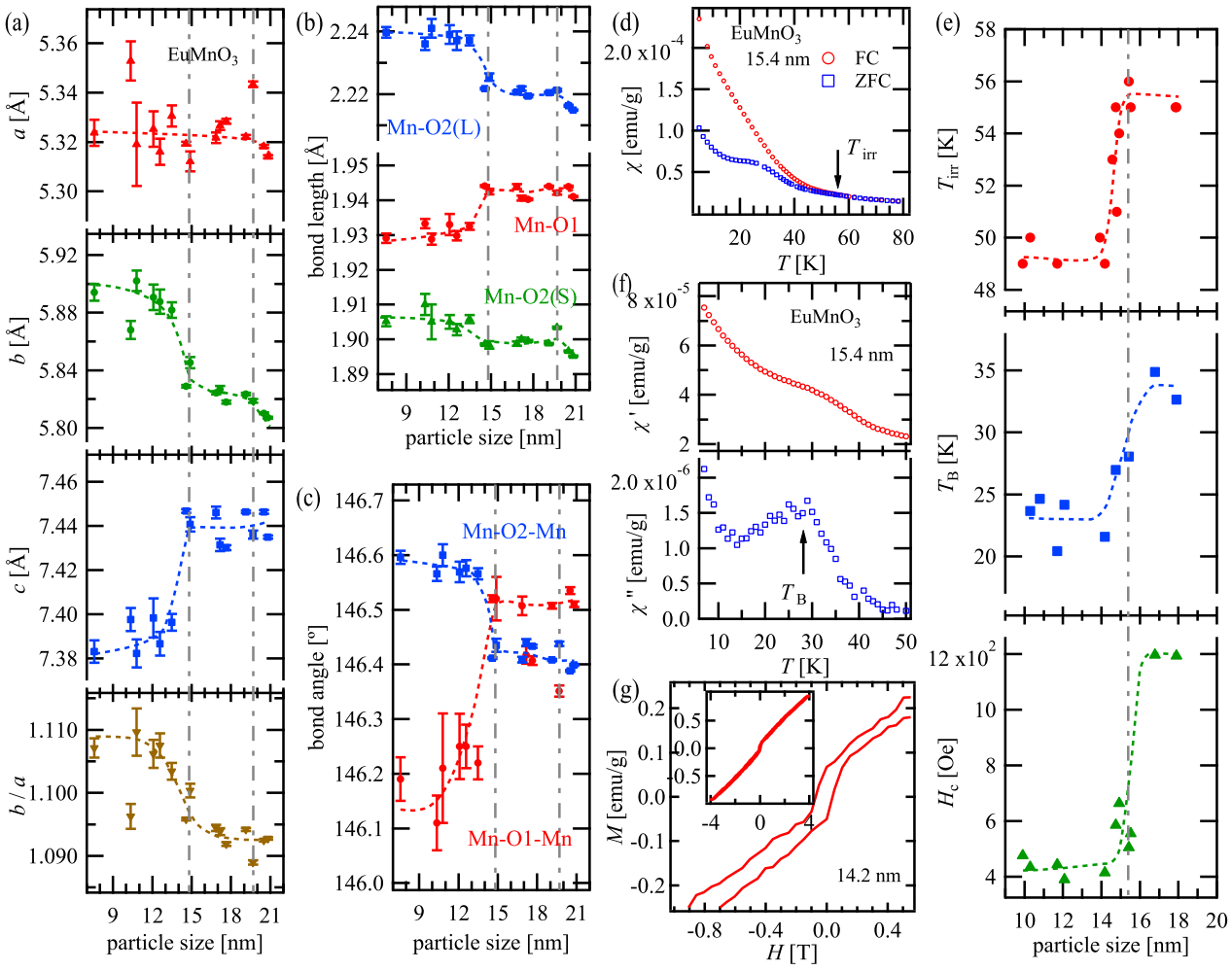

Figure 5: Particle size dependence of (a) lattice constants a, b, c, and b/a, (b) calculated Mn–O bond lengths, and (c) Mn–O–Mn bond angles (c) of the $EuMnO_3$ nanoparticles. Vertical dashed lines indicate the characteristic size, S_{c1}(Eu) = 19.7 nm and S_{c2}(Eu) = 14.8 nm. (d) Temperature dependence of DC magnetic susceptibilities of $EuMnO_3$ nanoparticles with a particle size of 15.4 nm in an external magnetic field of 100 Oe under FC and ZFC conditions. Arrow indicates the T_{irr}. (e) Particle size dependences of T_{irr}, T_B, and H_c of the $EuMnO_3$ nanoparticles. Vertical dashed lines indicate the characteristic size, S_m(Eu) = 15.3 nm. (f) Temperature dependence of χ' and $\chi''$of $EuMnO_3$ nanoparticles with a particle size of 15.4 nm at a frequency of 100 Hz in a zero DC field. Arrow indicates the T_B. (g) Magnetization curve up to 4 T of $EuMnO_3$ nanoparticles with particle size of 14.2 nm at 15 K.

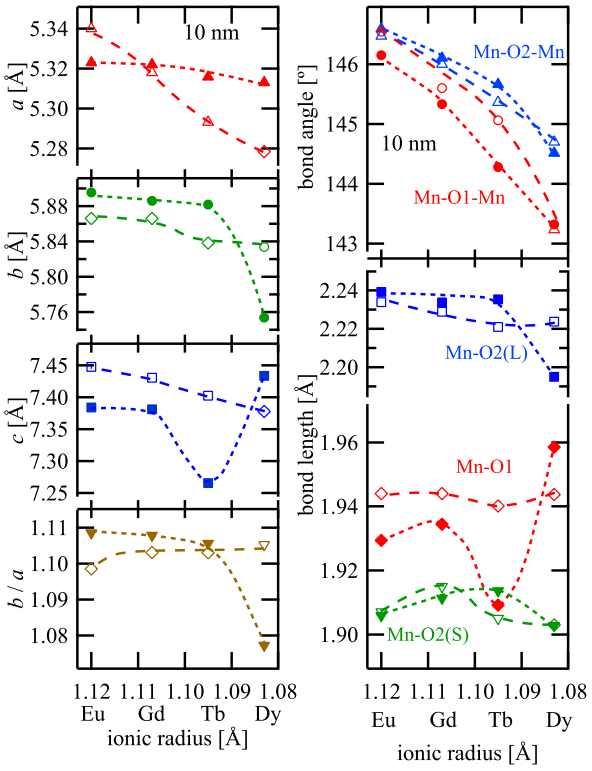

Figure 6: Lattice constants, Mn–O bond lengths, and Mn–O–Mn bond angles of nanoparticles with a particle size of 10 nm (solid symbols) and the bulk crystals (open symbols) as a function of the ionic radii of the lanthanoid ions. The values for the nanoparticles were extracted from their lattice parameters shown in Figs. 2 –5.

The correlation between magnetic properties and crystal structures was discussed in detail. The crystal lattice parameters (lattice constants, bond angles, and bond lengths) and magnetic properties (T_{irr}, T_{B}, and H_{c}) exhibited pronounced changes below the equivalent characteristic particle sizes, S_{c} and S_{m}. The $RMnO_3$ bulk crystals displayed a pronounced magnetic irreversibility between FC and ZFC susceptibilities below the incommensurate antiferromagnetic transition temperature $T_{\mathrm{N}}(\mathrm{Mn})$.[22] This suggests that the observed T_{irr} of the $RMnO_3$ nanoparticles corresponded to $T_{\mathrm{N}}(\mathrm{Mn})$. The change in T_{irr} corresponding to $T_{\mathrm{N}}(\mathrm{Mn})$ was qualitatively consistent with changes in the crystal lattice parameters. The size dependence of the orthorhombic distortion, Mn–O bond length, and Mn–O–Mn bond angles exhibited opposite tendencies for $DyMnO_3$ and the other three compounds. For $TbMnO_3$, $GdMnO_3$, and $EuMnO_3$ nanoparticles, the Mn–O1 decreased and the Mn–O2(L) and Mn–O2(S) increased with decreasing particle size below S_{c}, whereas those of $DyMnO_3$ nanoparticles exhibited opposite size dependence. That is, the MnO_6 octahedra of the $EuMnO_3$, $GdMnO_3$, and $TbMnO_3$ nanoparticles expanded along the *ab*-plane and contracted along the *c*-axis (tensile strain), whereas those of the $DyMnO_3$ nanoparticles compressed along the *ab*-plane and expanded along the *c*-axis (compressive strain), as shown by schematics in Fig. 8. As particle size decreased, the tensile and compress strain of the MnO_6 octahedra were enhanced below S_{c}. The results imply that the modulation of orthorhombic distortion, that is, Jahn–Teller distortion, of the nanoparticles was accompanied by changes in magnetic interactions as described later. Therefore, the sized dependence of T_{irr}, T_{B}, and H_{c} of $DyMnO_3$ nanoparticles exhibited opposite tendencies of those of the other three nanoparticles as well.

$EuMnO_3$, $GdMnO_3$, and $TbMnO_3$ nanoparticles with the tensile strain exhibited a higher $T_{\mathrm{N}}(\mathrm{Mn})$ than the corresponding bulk crystals above S_{c2}. Figure 7 shows the relationship between the orthorhombic distortion b/a, particle size, and lanthanoid ionic radius. The S_{m} occurred along the boundary of $b/a = 1.10$, except for $S_{\mathrm{m2}}(\mathrm{Dy}) = 8.2$ nm of the $DyMnO_3$ nanoparticles, regardless of the type of strain. This behavior suggests that changes in the

orthorhombic distortion determine the characteristic sizes of magnetic properties. The study of the $LaMnO_3$ film with epitaxial strain revealed a strong correlation between lattice strain and magnetic interactions.[28,31,33,36,56,57] Under high tensile strain, the x^2-y^2 orbital strengthened the double exchange interaction to stabilize the ferromagnetic ordering in the MnO_2 plane, while the double exchange interaction between the MnO_2 planes reduced because of the negligible occupation of the $3z^2-1$ orbital, which stabilized the A-AFM ordering. In contrast, under high compressive strain, the higher occupancy of the $3z^2-1$ orbital led to a ferromagnetic coupling between the MnO_2 planes, while the reduced x^2-y^2 occupancy induced antiferromagnetic ordering in the MnO_2 plane, stabilizing the C-type magnetic configuration. In addition, the theoretical study of magnetic exchange interactions in $RMnO_3$ revealed changes in the next-neighbor and next-nearest-neighbor interactions and magnetic phase diagram as a function of distortion of MnO_6 octahedra.[5,27,29,30,58] These results show that the changes in the magnetic interactions of the $EuMnO_3$, $GdMnO_3$, and $TbMnO_3$ nanoparticles are due to tensile strain, which led to a strengthening of the double exchange interaction, resulting in the stabilization of the A-type antiferromagnetic state and an increase in T_N(Mn) compared to that of the bulk crystal above S_{c2}. Below S_{c2}, the magnetic properties of the $EuMnO_3$ and $GdMnO_3$ nanoparticles did not exhibit significant contribution of ferromagnetic coupling, while the crystal lattice parameters were similar to those of the bulk crystals with smaller ionic radii. Therefore, below S_m(Eu) and S_{m2}(Gd), the magnetic state of the $EuMnO_3$ and $GdMnO_3$ nanoparticles change from an A-AFM ordered state to a cycloidal spin ordered state. In contrast, it is believed that the C-type or E-type antiferromagnetic state is stabilized in the $DyMnO_3$ nanoparticles, which displayed compressive strain. In addition, the Mn–O–Mn bond angles and Mn–O bond lengths of the $DyMnO_3$ nanoparticles with a particle size of 10 nm were similar to those of $ErMnO_3$ bulk crystals[7] with an E-type antiferromagnetic state. O. L. Makarova *et al.*[59] demonstrated that, in a neutron diffraction study of $TbMnO_3$ bulk crystal under high pressure, the modified structure induces commensurate order and changing the original incommensurate order with

microscopic changes in the exchange interactions. Under high pressure, the E-type commensurate spin structure is stabilized for Mn magnetic moments and change in the phase of the modulation between neighboring Mn chains and a reorientation of the Mn moments along a-axis. The E-type antiferromagnetic state is thought to be stabilized by lattice distortion in $DyMnO_3$ nanoparticles with particle size of smaller than $S_{m2}(Dy) = 8.2$ nm.

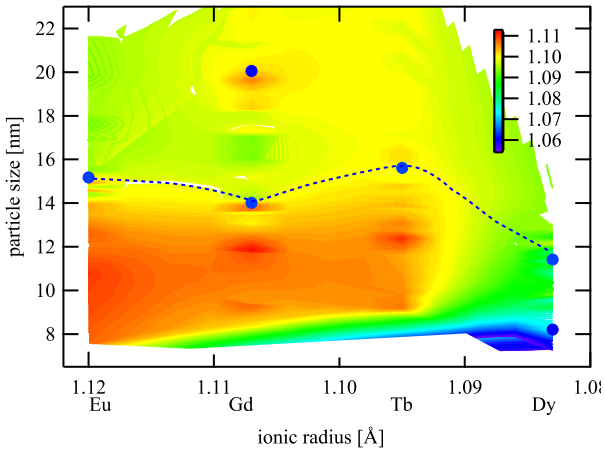

Figure 7: Contour plot of orthorhombic distortion b/a as a function of particle size and ionic radii of lanthanoid ion. The color change from red to blue indicates values of b/a ranging from 1.11 to 1.05. Circle indicate the magnetic characteristic size S_m determined by inflection points in the size dependences of the magnetic properties.

The magnetic phase diagram of the nanoparticles as a function of lanthanoid ionic radius and particle size was obtained from these results (Fig. 8). The value of T_{irr} was represented by a contour plot with change in color from red to blue. The $T_N(Mn)$ of the nanoparticles exhibited a significant reduction below S_{c1}. Both the S_c and S_m changed with lanthanoid ionic radius, while the S_c and S_m of the $DyMnO_3$ nanoparticles were significantly smaller than those of other three nanoparticles. $EuMnO_3$ and $GdMnO_3$ with an A-AFM phase have a phase boundary around S_{m2} (S_{c2}), where their magnetic phase changes to a cycloidal spin ordered state below the S_{c2} and S_{m2}. In contrast, for $DyMnO_3$, a phase boundary between the cycloid spin and the E-AFM state was observed at approximately S_{m2} (S_{c2}). The two phase transitions were attributed to the distortion of crystal structure owing to the decreasing particle size. The magnetic properties of the nanoparticles essentially followed

the magnetic phase diagram of the bulk crystals; however, the modulation of the structure by Jahn–Teller distortion caused changes in the magnetic interactions, which consequently affected the magnetic properties of the nanoparticles.

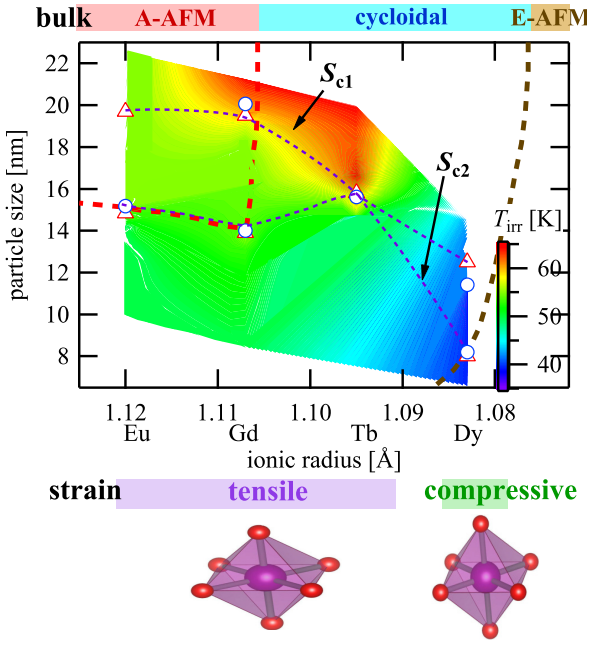

Figure 8: Magnetic phase diagram of the nanoparticles as a function of lanthanoid ionic radius and particle size at the lowest temperature. The magnetic phases of the bulk crystal at the lowest temperature is listed at the top of figure. The value of T_{irr} (i.e. T_{N}(Mn)) of the nanoparticles is represented by the color of the contour plot. Circles and triangles show the characteristic sizes of the magnetic properties (S_{m}) and that of the crystal structure (S_{c}), respectively, which indicate inflection points in the size dependence of magnetic properties and crystal lattice parameters, as shown in Figs. 2–5. The dashed line shows the phase boundaries between the A-AFM and the cycloid spin states, and between the cycloid spin and the E-AFM states. The nanoparticles with an A-AFM state exhibited a ferromagnetic-like behavior in DC susceptibilities. The type of strain experienced by the MnO_6 octahedra in the nanoparticles is listed and schematics of the MnO_6 octahedra with tensile and compressive strain were draw at the bottom of the phase diagram.

Conclusion

We synthesized $RMnO_3$ (R = Eu, Gd, Tb, and Dy) nanoparticles with particle sizes ranging from 6.5 to 23 nm. Subsequently, we investigated their crystal structures and magnetic

properties. The nanoparticles exhibited a strong correlation between crystal structure and magnetic properties, which depended on the particle size. Significant changes in the crystal lattice parameters at the characteristic sizes resulted in pronounced changes in the magnetic properties of the nanoparticles. The characteristic sizes depended on the lanthanoid ionic radius. The magnetic properties of all the nanoparticles correlated with the orthorhombic distortion (*i.e.*, Jahn–Teller distortion). The characteristic sizes of magnetic properties corresponded to the magnitude of the orthorhombic distortion $b/a = 1.10$, regardless of ionic radius. In addition, the size effects on the crystal structure and magnetic properties of the nanoparticles differed depending on the ionic radius of the lanthanoid. $EuMnO_3$, $GdMnO_3$, and $TbMnO_3$ nanoparticles exhibited tensile strain, whereas $DyMnO_3$ nanoparticles exhibited compressive strain. The magnetic properties of the $DyMnO_3$ exhibited different size dependences to those of the other nanoparticles. As particle size decreased, the values of the crystal lattice parameters of the nanoparticles were equivalent to those of bulk crystals with smaller ionic radii, resulting in a shift of the magnetic phase diagram to that of bulk crystals with smaller ionic radii, particularly in particles smaller than the characteristic size. The magnetic properties of the nanoparticles essentially followed the magnetic phase diagram of the bulk crystals, except for changes caused by modification of the crystal structure. Future work will focus on calculating the magnetic interactions based on the nanoparticle crystal structure to understand the relationship between magnetic properties, particle size, and lanthanoid ionic radii.

Acknowledgement

This work was supported by a Grant-in-Aid for Young Scientists (B) (No. 25870999) from the Ministry of Education, Culture, Sports, Science, and Technology of Japan and funding from Fukuoka University (Grant No.205003). The synchrotron radiation experiments were performed using the BL-8B beamline located at the Photon Factory (Proposal No. 2013G523,

2017G027, and 2019G039)

References

(1) Kimura, T.; Ishihara, S.; Shintani, H.; Arima, T.; Takahashi, K. T.; Ishizaka, K.; Tokura, Y. Distorted perovskite with e_g^1 configuration as a frustrated spin system. *Phys. Rev. B* **2003**, *68*, 060403(R).

(2) Goto, T.; Kimura, T.; Lawes, G.; Ramirez, A. P.; Tokura, Y. Ferroelectricity and Giant Magnetocapacitance in Perovskite Rare-Earth Manganites. *Phys. Rev. Lett.* **2004**, *92*, 257201.

(3) Ishiwata, S.; Kaneko, Y.; Tokunaga, Y.; Taguchi, Y.; Arima, T.; Tokura, Y. Perovskite manganites hosting versatile multiferroic phases with symmetric and antisymmetric exchange strictions. *Phys. Rev. B* **2010**, *81*, 100411(R).

(4) Mochizuki, M.; Furukawa, N.; Nagaosa, N. Theory of spin-phonon coupling in multiferroic manganese perovskites $RMnO_3$. *Phys. Rev. B* **2011**, *84*, 144409.

(5) Zhou, J.-S.; Goodenough, J. B. Unusual Evolution of the Magnetic Interactions versus Structural Distortions in $RMnO_3$ Perovskites. *Phys. Rev. Lett.* **2006**, *96*, 247202.

(6) Yamauchi, K.; Freimuth, F.; Blúgel, S.; Picozzi, S. Magnetically induced ferroelectricity in orthorhombic manganites: Microscopic origin and chemical trends. *Phys. Rev. B* **2008**, *78*, 014403.

(7) Alonso, J. A.; Martínez-Lope, M. J.; Casais, M. T.; Fernández-Díaz, M. T. Evolution of the Jahn-Teller Distortion of MnO_6 Octahedra in $RMnO_3$ Perovskites (R = Pr, Nd, Dy, Tb, Ho, Er, Y): A Neutron Diffraction Study. *Inorg. Chem.* **2000**, *39*, 917.

(8) Dabrowski, B.; Kolesnik, S.; Baszczuk, A.; Chmaissem, O.; Maxwell, T.; Mais, J. Struc-

tural,transport,and magnetic properties of $RMnO_3$ perovskites (R = La, Pr, Nd, Sm, ^{153}Eu, Dy). *J. Solid State Chem.* **2005**, *178*, 629.

(9) Mori, T.; Kamegashira, N.; Aoki, K.; Shishido, T.; Fukuda, T. Crystal growth and crystal structures of the $LnMnO_3$ perovskites: Ln = Nd, Sm, Eu and Gd. *Materials Lett.* **2002**, *54*, 238.

(10) Laverdière, J.; Jandl, S.; Mukhin, A. A.; Ivanov, V. Y.; Ivanov, V. G.; Iliev, M. N. Spin-phonon coupling in orthorhombic $RMnO_3$ (R = Pr, Nd, Sm, Eu, Gd, Tb, Dy, Ho, Y): A Raman study. *Phys. Rev. B* **2006**, *73*, 214301.

(11) Kajimoto, R.; Mochizuki, H.; Yoshizawa, H.; Shintani, H.; Kimura, T.; Tokura, Y. R-Dependence of Spin Exchange Interactions in $RMnO_3$ (R = Rare-Earth Ions). *J. Phys. Soc. Jpn.* **2005**, *74*, 2430.

(12) Goto, T.; Yamasaki, Y.; Watanabe, H.; Kimura, T.; Tokura, Y. Anticorrelation between ferromagnetism and ferroelectricity in perovskite manganites. *Phys. Rev. B* **2005**, *72*, 220403(R).

(13) Nomura, T.; Masuzawa, J.; Katsufuji, T. Dynamical specific heat of two-phase coexistence in $RMnO_3$. *Phys. Rev. B* **2006**, *74*, 220403(R).

(14) Yamasaki, Y.; Miyasaka, S.; Goto, T.; Sagayama, H.; Arima, T.; Tokura, Y. Ferroelectric phase transitions of 3d-spin origin in $Eu_{1-x}Y_xMnO_3$. *Phys. Rev. B* **2007**, *76*, 184418.

(15) Arima, T.; Tokunaga, A.; Goto, T.; Kimura, H.; Noda, Y.; Tokura, Y. Collinear to Spiral Spin Transformation without Changing the Modulation Wavelength upon Ferroelectric Transition in $Tb_{1-x}Dy_xMnO_3$. *Phys. Rev. Lett.* **2006**, *96*, 097202.

(16) Zhang, N.; Guo, Y. Y.; Lin, L.; Dong, S.; Yan, Z. B.; Li, X. G.; Liu, J.-M. Ho substi-

tution suppresses collinear Dy spin order and enhances polarization in $DyMnO_3$. *Appl. Phys. Lett.* **2011**, *99*, 102509.

(17) Pimenov, A.; Loidl, A.; Mukhin, A. A.; Travkin, V. D.; Ivanov, V. Y.; Balbashov, A. M. Terahertz spectroscopy of electromagnons in $Eu_{1-x}Y_xMnO_3$. *Phys. Rev. B* **2008**, *77*, 014438.

(18) Hemberger, J.; Lobina, S.; von Nidda, H.-A. K.; Tristan, N.; Ivanov, V. Y.; Mukhin, A. A.; Balbashov, A. M.; Loidl, A. Complex interplay of 3d and 4f magnetism in $La_{1-x}Gd_xMnO_3$. *Phys. Rev. B* **2004**, *70*, 024414.

(19) Hamdi, R.; Tozri, A.; Smari, M.; Dhahri, E.; Bessais, L. Structural, magnetic, magnetocaloric and electrical studies of $Dy_{0.5}(Sr_{1-x}Ca_x)_{0.5}MnO_3$ manganites. *J. Magn. Magn. Mater.* **2017**, *444*, 270.

(20) Harikrishnan, S.; Kumar, C. M. N.; Rao, S. S.; Bhat, H. L.; Bhat, S. V.; Elizabeth, S. Electron paramagnetic resonance studies on multiferroic $DyMnO_3$ and $Dy_{0.5}Sr_{0.5}MnO_3$. *J. Appl. Phys.* **2008**, *104*, 023902.

(21) Dagotto, E.; Hotta, T.; Moreo, A. COLOSSAL MAGNETORESISTANT MATERIALS: THE KEY ROLE OF PHASE SEPARATION. *Physics Reports* **2001**, *344*, 1.

(22) Ferreira, W. S.; Moreira, J. A.; Almeida, A.; Chaves, M. R.; Araújo, J. P.; Oliveira, J. B.; Silva, J. M. M. D.; Sá, M. A.; Mendonça, T. M.; ao Carvalho, P. S.; Kreisel, J.; Ribeiro, J. L.; Vieira, L. G.; Tavares, P. B.; Mendonça, S. Spin-phonon coupling and magnetoelectric properties: $EuMnO_3$ versus $GdMnO_3$. *Phys. Rev. B* **2009**, *79*, 054303.

(23) Kimura, T.; Lawes, G.; Goto, T.; Tokura, Y.; Ramirez, A. P. Magnetoelectric phase diagrams of orthorhombic $RMnO_3$ (R = Gd, Tb, and Dy). *Phys. Rev. B* **2005**, *71*, 224425.

(24) Kimura, T.; Goto, T.; Shintani, H.; Ishizaka, K.; Arima, T.; Tokura, Y. Magnetic control of ferroelectric polarization. *Nature* **2003**, *426*, 55.

(25) Tachibana, M.; Shimoyama, T.; Kawaji, H.; Atake, T.; Muromachi, E. T. Jahn-Teller distortion and magnetic transitions in perovskite $RMnO_3$ (R = Ho, Er, Tm, Yb, and Lu). *Phys. Rev. B* **2007**, *75*, 144425.

(26) Ishiwata, S.; Kaneko, Y.; Tokunaga, Y.; Taguchi, Y.; Arima, T. H.; Tokura, Y. Perovskite manganites hosting versatile multiferroic phases with symmetric and antisymmetric exchange strictions. *Phys. Rev. B* **2010**, *81*, 100411(R).

(27) Kim, B. H.; Min, B. I. Nearest and next-nearest superexchange interactions in orthorhombic perovskite manganites $RMnO_3$ (R = rare earth). *Phys. Rev. B* **2009**, *80*, 064416.

(28) K. Horiba, a. A. M.; Chikamatsu, A.; Yoshimatsu, K.; Kumigashira, H.; Wadati, H.; Fujimori, A.; Ueda, S.; Yoshikawa, H.; Ikenaga, E.; Kim, J. J.; Kobayashi, K.; Oshima, M. Microscopic model and phase diagrams of the multiferroic perovskite manganites. *Phys. Rev. B* **2009**, *80*, 132406.

(29) Dong, S.; Yu, R.; Yunoki, S.; Liu, J.-M.; Dagotto, E. Origin of multiferroic spiral spin order in the $RMnO_3$ perovskites. *Phys. Rev. B* **2008**, *78*, 155121.

(30) Mochizuki, M.; Furukawa, N.; Nagaosa, N. Theory of spin-phonon coupling in multiferroic manganese perovskites $RMnO_3$. *Phys. Rev. B* **2011**, *84*, 144409.

(31) Yamada, H.; Kawasaki, M. $LaMnO_3/SrMnO_3$ interfaces with coupled charge-spin-orbital modulation. *Appl. Phys. Lett.* **2006**, *89*, 052506.

(32) Lee, J.-H.; Murugavel, P.; Lee, D.; Noh, T. W.; Jo, Y.; Jung, M.-H.; Jang, K. H.; Park, J.-G. Multiferroic properties of epitaxially stabilized hexagonal $DyMnO_3$ thin films. *Appl. Phys. Lett.* **2007**, *90*, 012903.

(33) Kanki, T.; Tanaka, H.; Kawai, T. Anomalous strain effect in $La_{0.8}Ba_{0.2}MnO_3$ epitaxial thin film: Role of the orbital degree of freedom in stabilizing ferromagnetism. *Phys. Rev. B* **2001**, *64*, 224418.

(34) Lin, T. H.; Shih, H. C.; Hsieh, C. C.; Luo, C. W.; Lin, J.-Y.; Her, J. L.; Yang, H. D.; Hsu, C.-H.; Wu, K. H.; Uen, T. M.; Juang, J. Y. Strain-induced effects on antiferromagnetic ordering and magnetocapacitance in orthorhombic $HoMnO_3$ thin films. *J. Phys.: Condens. Matter* **2009**, *21*, 026013.

(35) Venkatesan, S.; Daumont, C.; Kooi, B. J.; Noheda, B.; Hosson, J. T. M. D. Nanoscale domain evolution in thin films of multiferroic $TbMnO_3$. *Phys. Rev. B* **2009**, *80*, 214111.

(36) Rubi, D.; de Graaf, C.; Daumont, C. J. M.; Mannix, D.; Broer, R.; Noheda, B. Ferromagnetism and increased ionicity in epitaxially grown $TbMnO_3$ films. *Phys. Rev. B* **2009**, *79*, 014416.

(37) Razavi, F. S.; Gross, G.; Habermeier, H.-U.; Lebedev, O.; Amelinckx, S.; Tendeloom, G. V.; Vigliante, A. Epitaxial strain induced metal insulator transition in $La_{0.9}Sr_{0.1}MnO_3$ and $La_{0.88}Sr_{0.1}MnO_3$ thin films. *Appl. Phys. Lett.* **2000**, *76*, 155.

(38) Tajiri, T.; Deguchi, H.; Kohiki, S.; Mito, M.; Takagi, S.; Tsuda, K.; Murakami, Y. Novel Size Effect of $LaMnO_{3+\delta}$ Nanocrystals Embeded in SBA-15 Mesoporous Silica. *J. Phys. Soc. Jpn.* **2006**, *75*, 113704.

(39) Tajiri, T.; Deguchi, H.; S. Kohiki, a. M. M.; Takagi, S.; Mitome, M.; Murakami, Y.; Kohno, A. Phase Separation in $La_{1-x}Sr_xMnO_{3+\delta}$ Nanocrystals Studied by Electron Spin Resonance. *J. Phys. Soc. Jpn.* **2008**, *77*, 074715.

(40) Tajiri, T.; Terashita, N.; Hamamoto, K.; Deguchi, H.; Mito, M.; Morimoto, Y.; Konishi, K.; Kohno, A. Size dependences of crystal structure and magnetic properties of $DyMnO_3$ nanoparticles. *J. Magn. Magn. Mater.* **2013**, *345*, 288.

(41) Tajiri, T.; Mito, M.; Deguchi, H.; Kohno, A. Magnetic properties of $GdMnO_3$ nanoparticles embedded in mesoporous silica. *Physica B* **2018**, *536*, 111.

(42) Tajiri, T.; Deguchi, H.; Mito, M.; Konishi, K.; Miyahara, S.; Kohno, A. Effect of size on the magnetic properties and crystal structure of magnetically frustrated $DyMn_2O_5$ nanoparticles. *Phys. Rev. B* **2018**, *98*, 064409.

(43) Tajiri, T.; Saisho, S.; Mito, M.; Deguchi, H.; Konishi, K.; Kohno, A. Size Dependence of Crystal Structure and Magnetic Properties of NiO Nanoparticles in Mesoporous Silica. *J. Phys. Chem. C* **2015**, *119*, 1194.

(44) Cai, X.; Shi, L.; Zhou, S.; Zhao, J.; Guo, Y.; Wang, C. Size-dependent structure and magnetic properties of $DyMnO_3$ nanoparticles. *J. Appl. Phys.* **2014**, *116*, 103903.

(45) Hamdi, R.; Tozri, A.; Smari, M.; Nouri, K.; Dhahri, E.; Bessais, L. Structural, magnetic and AC susceptibility properties of $Dy_{0.5}(Sr_{1-x}Ca_x)_{0.5}MnO_3$ ($0 \leq x \leq 0.3$) manganites. *J. Mole. Struct.* **2019**, *1175*, 844.

(46) Wang, X. L.; Li, D.; Cui, T. Y.; Kharel, P.; Liu, W.; Zhang, Z. D. Magnetic and optical properties of multiferroic $GdMnO_3$ nanoparticles. *J. Appl. Phys* **2010**, *107*, 09B510.

(47) Singh, D.; Gupta, R.; Bamzai, K. K. Electrical and magnetic properties of $GdCr_xMn_{1-x}O_3$ ($x = 0.0, 0.1$) multiferroic nanoparticles. *J. Mater. Sci. Mater. Electron* **2017**, *28*, 5295.

(48) Negi, P.; Dixit, G.; Agrawal, H. M.; Srivastava, R. C. Structural, Optical and Magnetic Properties of Multiferroic $GdMnO_3$ Nanoparticles. *J. Supercond. Nov. Magn.* **2013**, *26*, 1611.

(49) Rasras, A.; Hamdi, R.; Mansour, S.; Samara, A.; Haik, Y. Study of the magnetocaloric effect in single-phase antiferromagnetic $GdMnO_3$. *J. Phys. Chem. Solids* **2021**, *149*, 109798.

(50) Kharrazi, S.; Kundaliya, D. C.; Gosavi, S. W.; Kulkarni, S. K.; Venkatesan, T.; Ogale, S. B.; J. Urban, S. P.; Cheong, S.-W. Multiferroic $TbMnO_3$ nanoparticles. *Solid State Comm.* **2006**, *138*, 395.

(51) Das, R.; Jaiswal, A.; Adyanthaya, S.; Poddar, P. Effect of particle size and annealing on spin and phonon behavior in $TbMnO_3$. *J. Appl. Phys.* **2011**, *109*, 064309.

(52) Khule, S. M.; Acharya, S. A. Synthesis and magnetic properties of $TbMnO_3$ nanorods. *J. Exp. Nano.* **2013**, *8*, 288.

(53) Zhao, D.; Feng, J.; Huo, Q.; Melosh, N.; Fredrickson, G. H.; Chemlka, B. F.; Stucky, G. D. Triblock Copolymer Syntheses of Mesoporous Silica with Periodic 50 to 300 Angstrom Pores. *Science* **1998**, *279*, 548.

(54) Mori, T.; Aoki, K.; kamegashira, N.; Shishido, T.; Fukuda, T. Crystal structure of $DyMnO_3$. *Materials Lett.* **2000**, *42*, 387.

(55) Tadic, M.; Kralj, S.; Jagodic, M.; Hanzel, D.; Makovec, D. Magnetic properties of novel superparamagnetic iron oxide nanoclusters and their peculiarity under annealing treatment. *Applied Surface Science* **2014**, *322*, 255.

(56) Nanda, B. R. K.; Satpathy, S. Effects of strain on orbital ordering and magnetism at perovskite oxide interfaces: $LaMnO_3/SrMnO_3$. *Phys. Rev. B* **2008**, *78*, 054427.

(57) Zhang, J.; Tanaka, H.; Kanki, T.; Choi, J.-H.; Kawai, T. Strain effect and the phase diagram of $La_{1-x}Ba_xMnO_3$ thin films. *Phys. Rev. B* **2001**, *64*, 184404.

(58) Mochizuki, M.; Furukawa, N. Microscopic model and phase diagrams of the multiferroic perovskite manganites. *Phys. Rev. B* **2009**, *80*, 134416.

(59) Makarova, O. L.; Mirebeau, I.; Kichanov, S. E.; Rodriguez-Carvajal, J.; Forget, A. Pressure-induced change in the magnetic ordering of $TbMnO_3$. *Phys. Rev. B* **2011**, *84*, 020408.

TOC Graphic

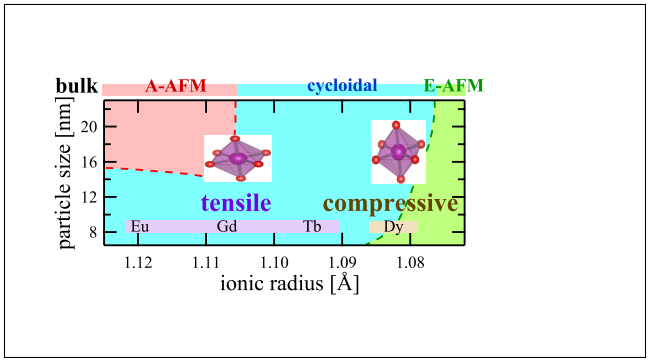
bulk
A-AFM
cycloidal
E-AFM
particle size [nm]
20
16
12
8
tensile
compressive
Eu
Gd
Tb
Dy
1.12
1.11
1.10
1.09
1.08
ionic radius [Å]